Pergamon

Int. J. Heat Mass Transfer. Vol. 41, No. 16, pp. 2485–2502, 1998

Printed in Great Britain
0017–9310/98 $19.00+0.00

PII: S0017-9310(97)00327-X

An investigation of the solutal, thermal and flow fields in unidirectional alloy solidification

JAMES E. SIMPSON and SURESH V. GARIMELLA†
Department of Mechanical Engineering, University of Wisconsin-Milwaukee, P.O. Box 784,
Milwaukee, WI 53201, U.S.A.

(*Received* 26 *June* 1997 *and in final form* 8 *October* 1997)

Abstract—Unidirectional solidification of a dilute alloy (tin-bismuth) in a two-dimensional rectangular cavity is investigated using a uniform computational grid. The energy equation is solved for the temperature field, while the species equation is solved for the solute distribution. A vorticity–vector potential representation is used for the governing equations for the velocity field. The constitutive equations are solved using a true transient method. An Alternating Direction Implicit (ADI) approximation is employed in the solution scheme for the vorticity while the conjugate gradient method is used for the vector potential equation. The results obtained from the numerical simulations compare very well with experimental and numerical results for directional solidification in the literature in terms of the propagation of the solidification front as well as the free convection flow patterns in the liquid. © 1998 Elsevier Science Ltd. All rights reserved.

1. INTRODUCTION

A growing number of theoretical and numerical analyses of solidification processes have been appearing in the literature. Unidirectional solidification has been particularly studied due to the improved material properties that can result. There is a continued need, however, to investigate these processes, especially when alloy solidification is considered. The aim of the present work is to develop an efficient methodology which can account for melt convection, as well as interface tracking and the application of realistic interface boundary conditions, while keeping computational costs low.

The solidification of aqueous salt solutions has been extensively investigated using both experimental and numerical approaches. Such systems behave in a manner analogous to metallic alloy melts and have the advantage of being transparent so that the interface propagation may be visualized. Zeng and Faghri [1, 2] reviewed numerical studies in this area; experimental studies are discussed in Garimella *et al.* [3].

Unlike aqueous systems, metallic melts are characterized by low Prandtl numbers, which poses significant difficulties for numerical solution. Among the first experiments to simulate directional solidification of low Prandtl number melts were those reported by Wolff and Viskanta [4]. They also obtained numerical results through a simplified formulation for comparison against their experiments for the solidification of pure tin. Raw and Lee [5] used a single-domain approach and a fixed grid to numerically simulate this problem. They solved a vorticity–vector potential representation of the constitutive equations along with an advanced weighting scheme that enabled the melt and solid to be treated as a single domain. Their results show superior agreement with experiment relative to the numerical investigations in [4]. Recently, an adaptive-grid numerical algorithm was developed [6] to solve for pure-material solidification, which involves explicitly tracking the front location and re-mapping the grid so that it conforms to the front location at each time interval. This explicit handling of the front comes at a high computational expense. Single-domain methods, such as the enthalpy method, are less expensive and implicitly track the interface location, recovering its location *a posteriori* from the solution procedure.

In alloy systems, both liquid and solid phases coexist over a range of temperatures and solute concentrations. The interface is thus no longer a distinct, sharp front, due to the dependence of freezing temperature on solute concentration. The region of interspersed solid and liquid is referred to as a mushy zone. Most alloy systems (and indeed, some pure materials when subject to undercooling) exhibit a mushy zone during solidification. The interfaces in the mushy zone become so complex that a two-domain approach is simply not feasible [1]. There are various treatments of the mushy zone in the literature. These treatments may be generally categorized under continuum approaches based on well-established mixture theories

---

† Author to whom correspondence should be addressed. Tel.: 001 414 229 6535. Fax: 001 414 229 6958. E-mail: sureshg@csd.uwm.edu.

NOMENCLATURE

A	area
AR	aspect ratio, H/L
c_p	specific heat capacity at constant pressure
C	species concentration
D	species diffusion coefficient
E	energy
f	volume fraction
g	acceleration due to gravity
Gr	Grashof number, $g\beta_T(T_H - T_C)L^3/v^2$
Gr_s	solutal Grashof number, $g\beta_c \Delta C^* L^3/v^2$
h	specific enthalpy
H	cavity height
k	thermal conductivity
K	segregation coefficient
L	cavity length
Le	Lewis number, α/D
m	slope of liquidus line, dT/dC
P	pressure
Pr	Prandtl number, v/α
$\tilde{q}$	heat flux vector
$\tilde{q}_c$	mass flux vector
rhs_{ij}	coefficient matrix in equation (28)
R_B	buoyancy ratio, Gr/Gr_s
Ra	Rayleigh number, $Gr\,Pr$
Ra_s	solutal Rayleigh number, $Gr_s\,Pr$
RHS_{ij}	coefficient matrix in equation (21)
t	time
T	temperature
u, v	velocity.

Greek symbols

α	thermal diffusivity
α_{ij}	coefficient matrix in equation (26)
β	expansion coefficient
γ	solidification front orientation
ΔC^*	concentration difference, $C_0^*(1-K)/K$
ΔT	$T_H - T_C$
ΔH	enthalpy of freezing
ζ	vorticity
θ	nondimensional temperature, $(T-T_C)/(T_H-T_C)$
Θ	nondimensional temperature, $(T-T_m)/(T_H-T_m)$
λ	nondimensional temperature, $c_p(T-T_m)/\Delta H$
Λ_{ij}	coefficient matrix in equation (28)
v	kinematic viscosity
ρ	density
ϕ	nondimensional enthalpy, $(h-h_m)/\Delta H$
ψ	stream function.

Subscripts

0	initial condition
C	located at cold wall
H	located at hot wall
i, j	located at i, jth finite-volume center
I, J	located at I, Jth finite-difference mesh point
L	liquid
m	at solidification front
mix	mixture
S	solid
wall	located at the boundary.

Superscripts

$\hat{}$	unit vector
$\tilde{}$	vector
$*$	reference or dimensional quantity
n	time step n.

[7] or local averaging approaches [8, 9]. Hyun *et al.* [10] recently simulated thermal and concentration-driven natural convection in a low-Prandtl number fluid at moderate Rayleigh numbers but their study did not include solidification.

The present study is the first step in creating a new generalized numerical model for the solution of alloy solidification for metallic systems including the full effects of thermosolutal convection. For this initial work, we consider the simplified case where the mushy zone is negligibly small and may be collapsed to a single, sharp interface. The aim of this paper is to present results for the directional solidification of a simple binary alloy at a low Prandtl number and high Rayleigh number, including the full effects of thermal and solutal-driven buoyancy.

2. MATHEMATICAL FORMULATION

2.1. *Vorticity–vector potential equations*

The thermosolutal buoyancy-driven motion of a viscous heat-conducting fluid contained in a rectangular box is modeled as shown in Fig. 1. The fluid is considered subject to the Boussinesq approximation. One side wall of the box is at a constant hot temperature (T_H) while the opposing wall is at a constant cold temperature (T_C). The top and bottom walls are considered adiabatic. The conservation of momentum

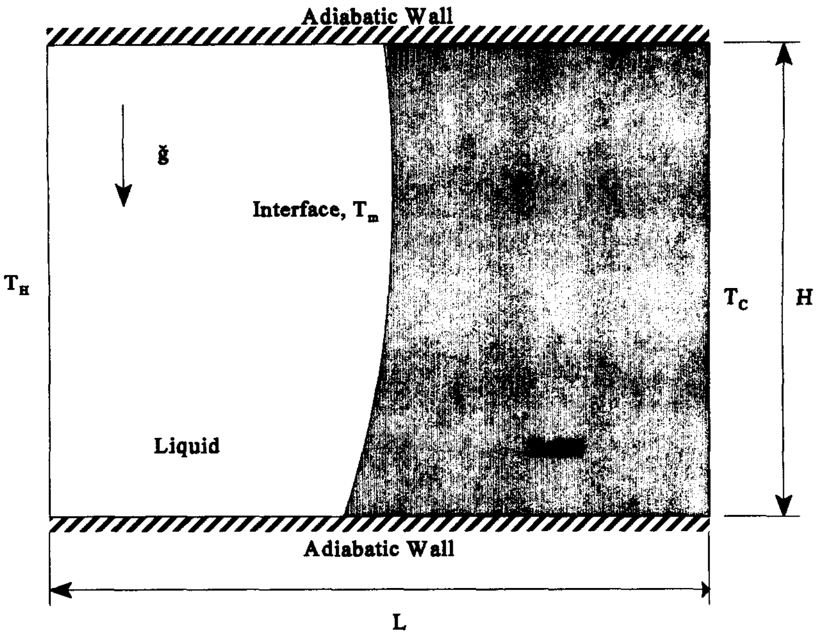

Fig. 1. Computational domain.

and mass are then expressed as two nonlinear, second order partial differential equations [11]:

$$\frac{\partial \vec{u}}{\partial t}+(\nabla\times\vec{u})\times\vec{u} = -[\beta_T(T-T_C)+\beta_C(C^*-C_0^*)]\vec{g} - \frac{1}{\rho_0}\nabla P+\nu\nabla^2\vec{u} \quad (1)$$

$$\nabla\cdot\vec{u}=0. \quad (2)$$

In nondimensionalizing these equations (definitions in the nomenclature), the reference density is calculated at T_C. Due to the low Prandtl number and high Rayleigh number of the flow under consideration, the appropriate reference quantities for nondimensionalizing velocity and time are

$$t^*=\frac{L^2}{\nu} \quad v^*=\nu\frac{Gr^{1/2}}{L}. \quad (3)$$

The nondimensional solute concentration is

$$C=\frac{C^*-C_0^*}{\Delta C^*}. \quad (4)$$

The nondimensionalization of equations (1) and (2) is, thus,

$$\frac{\partial \vec{u}}{\partial t}+Gr^{1/2}(\nabla\times\vec{u})\times\vec{u} = -Gr^{1/2}\,\theta\hat{g}-\frac{Gr_s}{Gr^{1/2}}C\hat{g}-Gr^{1/2}\,\nabla P+\nabla^2\vec{u}. \quad (5)$$

Equations (2) and (5) may be re-cast in terms of the derived variables, vorticity and vector potential:

$$\frac{\partial\tilde{\zeta}}{\partial t}+Gr^{1/2}\,\nabla\times(\tilde{\zeta}\times\vec{u}) = -Gr^{1/2}(\nabla\times\theta\hat{g})-\frac{Gr_s}{Gr^{1/2}}(\nabla\times C\hat{g})+\nabla^2\tilde{\zeta} \quad (6)$$

where the definitions of vorticity and stream function

$$\tilde{\zeta}=-\nabla\times\vec{u}, \quad \nabla^2\tilde{\psi}=-\tilde{\zeta} \quad (7)$$

result in

$$\vec{u}=\nabla\times\tilde{\psi}. \quad (8)$$

For convenience, we define the buoyancy ratio as

$$R_B=\frac{Gr_s}{Gr}=\frac{\beta_C\,\Delta C^*}{\beta_T\,\Delta T}. \quad (9)$$

Thus, equation (6) becomes

$$\frac{\partial\tilde{\zeta}}{\partial t}+Gr^{1/2}\,\nabla\times(\tilde{\zeta}\times\vec{u}) = -Gr^{1/2}(\nabla\times\theta\hat{g})-R_B\,Gr^{1/2}(\nabla\times C\hat{g})+\nabla^2\tilde{\zeta}. \quad (10)$$

As can be seen from equation (10), the inclusion of $Gr^{1/2}$ into the reference velocity has led to the convective and buoyancy terms being weighted by $Gr^{1/2}$, while the coefficient for the transient term remains at unity. The selection of this characteristic velocity has the effect of stabilizing the solution of the vorticity transport equation at large Grashof numbers, since the numerical values of velocity are kept small. The solution of equation (10) subject to equation (7) constitutes the vorticity–vector potential formulation of equations (1) and (2) for natural convection under conditions of high Grashof and low Prandtl numbers.

An appropriate set of boundary conditions needs to be specified for the physical domain shown in Fig. 1. For a non-slip wall, the boundary conditions to be imposed on vorticity and vector potential are described in Mallinson and de Vahl Davis [12]: the velocity is zero as are the tangential derivatives of its components. This leads to the following conditions for vorticity

$$x=0 \quad \begin{aligned} \zeta_1 &= 0 \\ \zeta_2 &= -\frac{\partial w}{\partial x} \\ \zeta_3 &= \frac{\partial v}{\partial x}. \end{aligned} \tag{11}$$

The vector potential at a plane, impermeable surface is normal to the surface and its gradient is zero:

$$x=0 \quad \begin{aligned} \frac{\partial \psi_1}{\partial x} &= 0 \\ \psi_2 &= 0 \\ \psi_3 &= 0. \end{aligned} \tag{12}$$

The boundary conditions for the other surfaces result from similar considerations [12]. As an initial condition, the fluid must be quiescent:

$$t=0 \quad \tilde{\psi} = \tilde{\zeta} = 0.$$

2.2. *The energy equation*

The nondimensionalized form of the governing equation for the conservation of energy is

$$\frac{\partial \theta}{\partial t} + Gr^{1/2}\,\nabla\cdot(\tilde{u}\theta) = \frac{1}{Pr}\nabla^2\theta. \tag{13}$$

An initial temperature equal to the hot wall temperature is applied throughout the flow field. At the boundaries, either a temperature or a heat flux at the surface is specified, viz.

$$\begin{aligned} \theta &= 1 \quad t=0 \\ \theta &= 1 \quad x=0 \\ \theta &= 0 \quad x=L \\ \partial\theta/\partial y &= 0 \quad y=0 \\ \partial\theta/\partial y &= 0 \quad y=H. \end{aligned} \tag{14}$$

In principle, the solution of the energy equation (13) coupled with the solution of the vorticity–vector potential equations (10), (7) and (8) would yield the temperature and velocity distribution throughout the simulation domain. However, the problem of modeling the physics of the propagation of the solidification front and determining its location remains to be addressed. We choose to do this by the robust and efficient enthalpy method [13], which is briefly discussed in Section 3.2. The constitutive equation required for this method is the integral equation describing the conservation of energy in an arbitrary control volume:

$$\int_t^{t+\Delta t} \frac{\partial}{\partial t}\left(\int_V E\,\mathrm{d}V\right)\mathrm{d}t = \int_t^{t+\Delta t}\int_A -\tilde{q}\cdot\hat{n}\,\mathrm{d}A\,\mathrm{d}t \tag{15}$$

where $\tilde{q}$ is the combined diffusion and convection energy flux vector and E is the total energy contained within the volume of integration.

2.3. *Solutal concentration equation*

The nondimensionalized equation for the conservation of solute throughout the computational domain is

$$\frac{\partial C}{\partial t} + Gr^{1/2}\,\nabla\cdot(\tilde{u}C) = \frac{1}{Le\,Pr}\nabla^2 C. \tag{16}$$

This equation is analogous to the energy equation. We impose an initial solute concentration throughout the solution domain. At the boundaries we demand that there be no flux of solute: no solute may exit the solution domain. Thus,

$$\begin{aligned} t=0 &\quad C=C_0 \\ x=0,L &\quad \partial C/\partial x = 0 \\ y=0,H &\quad \partial C/\partial y = 0. \end{aligned} \tag{17}$$

Again, in principle, solution of equation (16) along with energy equation (15) and vorticity–vector potential equations (10), (7) and (8) all subject to the relevant boundary and initial conditions are enough to determine the solute, temperature and velocity values throughout the solution domain. However, the more general problem involving phase change demands that the thermodynamics of solute redistribution be addressed. The methodology for this is described in the next section. The constitutive equation for this method uses the integral form of equation (16),

$$\int_t^{t+\Delta t} \frac{\partial}{\partial t}\left(\int_V C_{\mathrm{mix}}\,\mathrm{d}V\right)\mathrm{d}t = \int_t^{t+\Delta t}\int_A -\tilde{q}_{\mathrm{c}}\cdot\hat{n}\,\mathrm{d}A\,\mathrm{d}t \tag{18}$$

in which C_{mix} is the total solute mass within the volume of integration and $\tilde{q}_{\mathrm{c}}$ includes both convective and diffusive species fluxes.

3. NUMERICAL ANALYSIS

3.1. *Vorticity and vector potential*

The computational domain is primarily discretized using regularly spaced finite-difference mesh points. Superimposed on this grid are finite volumes which are required for the enthalpy method. The finite-volume centers are staggered with respect to the finite-difference mesh point locations. Vorticity, velocity and vector potentials are calculated at the finite-difference mesh points. Temperature, solute concentration and

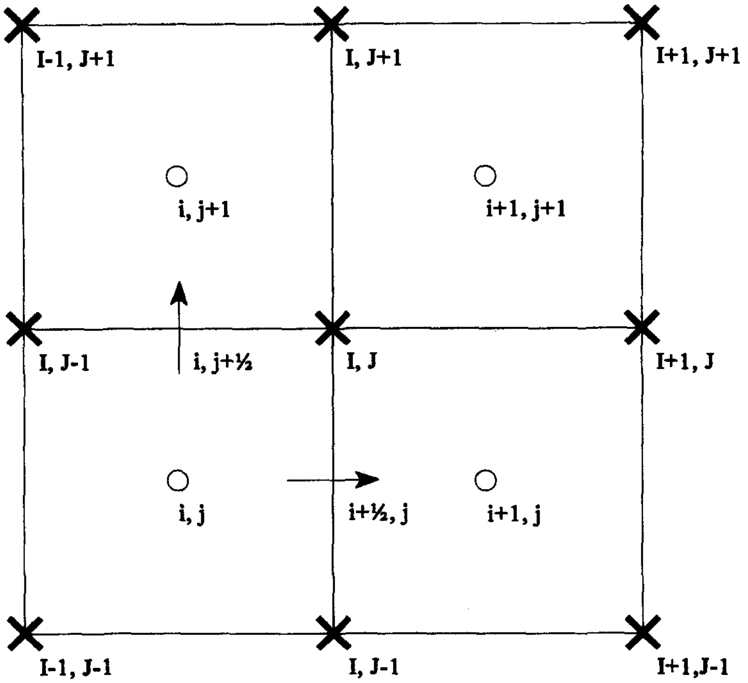

Fig. 2. Discretization scheme. Crosses represent locations for finite-difference calculations for the vorticity and vector potential equations; circles represent the centers of control volumes used for the energy and species equations. Simple linear interpolation is used to calculate the velocities at the control-volume faces.

enthalpy are evaluated at the control volume centers as a result of the solution of equations (15) and (18). This arrangement is shown in Fig. 2. The finite-volumes were staggered with respect to the finite-difference mesh points so that the most accurate values for velocity at the finite-volume faces could be obtained. These velocity values are required for the calculation of convective fluxes in the energy and species transport equations (Sections 3.2 and 3.3).

The discretization and solution schemes are explained in Simpson and Garimella [14]. The approach used here is modified from a program [15] written for the solution of natural convection in a rectangular cavity. The essential details are that the vorticity transport equation (10) and the vector potential equation (7) are discretized in space using the regular finite difference mesh. The discretized equation for the vorticity transport equation is solved using an Alternative Direction Implicit (ADI) scheme [16]. The discretized equation for vector potential is solved using the conjugate gradient method. This is a semi-iterative method used to solve specific systems of linear equations. The method is not discussed here, except to note that the values for vector potential at the previous time step are used as the initial guess values. Once the values of vector potential are known, the nodal velocities can be determined from equation (8).

It should be noted that while governing equations (10) and (7) are presented in three dimensions and the code is capable of solving for the flow field in 3-D, the simulations in this paper are restricted to two dimensions. This is accomplished by solving only the z-component of vorticity and vector potential and thus, yielding the requisite u- and v-velocity components.

3.1.1. *A note on the handling of boundary conditions.* The major difficulty in the solution procedure is the method by which matching conditions at the solid/liquid interface are posed. An additional complexity is introduced in this instance since the vorticity–vector potential statement of the constitutive equations is used, with the consequential increase in difficulty of stating the boundary conditions at a solid wall (Section 2.1). The method employed in the current solution scheme is similar to that described in [17] as the 'velocity switch-off method'. Since the solution scheme for the velocity field operates on the finite-difference mesh points, the aim is to determine which mesh points are in the solid domain, which lie in the liquid domain, and which can be declared to lie on the surface. To achieve this end, a 'liquid fraction' at the finite-difference mesh points is calculated from the average of the values in the four neighboring control volumes. The mesh point is considered liquid if this calculated value is greater than zero, and solid otherwise. Boundary points then exist at mesh points which are defined as solid adjacent to a mesh point which is defined as liquid. As shown in Fig. 3, the slope at which the interface is oriented is found as a consequence of a Hirt and Nichols [18] type front reconstruction; the boundary conditions may then be applied (following refs. [5, 19]) as

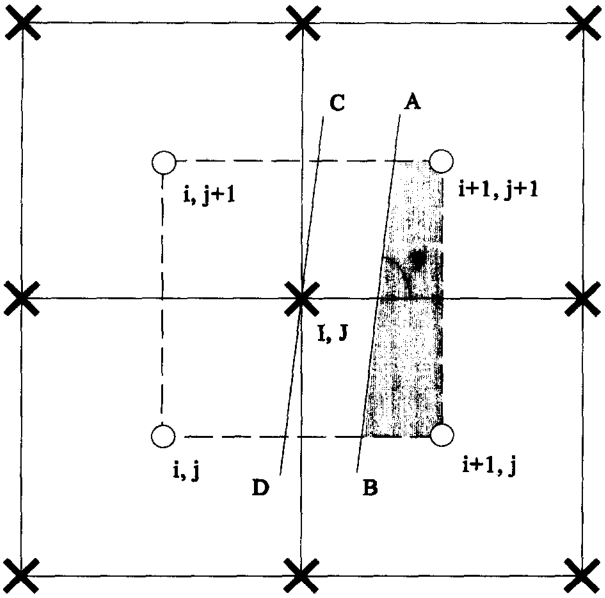

Fig. 3. Details of front reconstruction. Following Hirt and Nichols [18], the interface is considered to be planar in each cell (line AB). For simplicity, vorticity boundary conditions are applied on the fixed mesh point at the center of the cell (i.e. using line CD), irrespective of where the interface lies within the cell.

$$\psi_3 = 0$$

$$\zeta_3 = (\cos^{-2}\gamma)\,\partial^2\psi_3/\partial y^2 = (\sin^{-2}\gamma)\partial^2\psi_3/\partial x^2. \tag{19}$$

The slope of the interface is used to determine which of the two formulations for vorticity at the boundary is used. If the line is more horizontal than vertical then the first formulation is used and the converse applies.

3.2. *Energy equation*

The integral energy equation (15) is discretized using the finite-volume mesh. An upwind scheme is incorporated for the treatment of convective heat fluxes. This discretization may then be written as

$$\begin{aligned}
&\frac{\phi_{ij}^{n+1}-\phi_{ij}^{n}}{\Delta t}\Delta x\,\Delta y \\
&= Gr^{1/2}\,\Delta y[\lambda_{i,j}^{n+1}[\![u_{i-(1/2),j},0]\!]-\lambda_{i-1,j}^{n+1}[\![-u_{i-(1/2),j},0]\!] \\
&\quad+\lambda_{i,j}^{n+1}[\![-u_{i+(1/2),j},0]\!]-\lambda_{i+1,j}^{n+1}[\![u_{i+(1/2),j},0]\!]] \\
&\quad+Gr^{1/2}\,\Delta x[\lambda_{i,j}^{n+1}[\![u_{i,j-(1/2)},0]\!]-\lambda_{i,j-1}^{n+1}[\![-u_{i,j-(1/2)},0]\!] \\
&\quad+\lambda_{i,j}^{n+1}[\![-u_{i,j+(1/2)},0]\!]-\lambda_{i,j+1}^{n+1}[\![u_{i,j+(1/2)},0]\!]] \\
&\quad+\frac{1}{Pr}\Delta y[k_{i+(1/2),j}(\lambda_{i+1,j}^{n+1}-\lambda_{i,j}^{n+1})/\Delta x \\
&\quad-k_{i-(1/2),j}(\lambda_{i,j}^{n+1}-\lambda_{i-1,j}^{n+1})/\Delta x] \\
&\quad+\frac{1}{Pr}\Delta x[k_{i,j+(1/2)}(\lambda_{i,j+1}^{n+1}-\lambda_{i,j}^{n+1})/\Delta y \\
&\quad-k_{i,j-(1/2)}(\lambda_{i,j}^{n+1}-\lambda_{i,j-1}^{n+1})/\Delta y]
\end{aligned} \tag{20}$$

in which $[A, B]$ is the maximum of A and B. The velocities at the finite-volume faces are the interpolated values from the finite-difference mesh points. As stated earlier, the finite-volume mesh was staggered with respect to the finite-difference mesh (as shown in Fig. 2) in order to obtain the most accurate interpolated values.

The enthalpy method is the solution scheme for equation (15). The thrust of the method is to use equation (15) to determine the cell temperature and enthalpy. The complete methodology for the solution is explained in [14]; a brief outline is provided here. Essentially, equation (20) is advanced forward in time using Gauss–Seidel iteration with successive over relaxation. For this method, equation (20) reduces to

$$\phi_{i,j}^{p+1} + C_{i,j}^{p}\lambda_{i,j}^{p+1} = RHS_{i,j}^{p} \tag{21}$$

in which p denotes the inner iteration number, and the values at time step n are used as the first approximation. The *RHS* is fully explicit at iteration p. The relationship between temperature and enthalpy gives us

$$\phi_{i,j}^{p+1} = \begin{cases} \dfrac{RHS_{i,j}^{p}}{C_{i,j}^{p}+1} & \text{if } RHS_{i,j}^{p} \leqslant 0 \\ 0 & \text{if } 0 < RHS_{i,j}^{p} < 1 \\ \dfrac{RHS_{i,j}^{p}+C_{i,j}^{p}}{C_{i,j}^{p}+1}, & \text{if } RHS_{i,j}^{p} \geqslant 1 \end{cases} \tag{22}$$

with corresponding results for the temperature (λ). Iterations proceed until convergence, at which time the new values at time step $(n+1)$ for temperature and enthalpy are declared to be those found at convergence. Convergence is assessed in the usual manner with a tolerance of 10^{-6}. In cells which contain the interface, the cell enthalpies are equivalent to the cell liquid fractions by virtue of our non-dimensionalization scheme. In this way, the approximate location of the solidification front is determined *a posteriori* from this solution scheme, using Hirt and Nichols [18] reconstruction.

3.3. *Solutal concentration equation*

The discretized analog of equation (18) is

$$\frac{C^{n+1}_{\mathrm{mix},ij} - C^{n}_{\mathrm{mix},ij}}{\Delta t} \Delta x \, \Delta y$$

$$= Gr^{1/2}\,\Delta y[C^{n+1}_{\mathrm{L},i,j}[\![u_{i-(1/2),j}, 0]\!] - C^{n+1}_{\mathrm{L},i-1,j}[\![-u_{i-(1/2),j}, 0]\!]$$

$$+ C^{n+1}_{\mathrm{L},i,j}[\![-u_{i+(1/2),j}, 0]\!] - C^{n+1}_{\mathrm{L},i+1,j}[\![u_{i+(1/2),j}, 0]\!]]$$

$$+ Gr^{1/2}\,\Delta x[C^{n+1}_{\mathrm{L},i,j}[\![u_{i,j-(1/2)}, 0]\!] - C^{n+1}_{\mathrm{L},i,j-1}[\![-u_{i,j-(1/2)}, 0]\!]$$

$$+ C^{n+1}_{\mathrm{L},i,j}[\![-u_{i,j+(1/2)}, 0]\!] - C^{n+1}_{\mathrm{L},i,j+1}[\![u_{i,j+(1/2)}, 0]\!]]$$

$$+ \frac{1}{Le\,Pr}\Delta y\left[D_{i+(1/2),j}\frac{C^{n+1}_{\mathrm{L},i+1,j} - C^{n+1}_{\mathrm{L},i,j}}{\Delta x}\right.$$

$$\left. - D_{i-(1/2),j}\frac{C^{n+1}_{\mathrm{L},i,j} - C^{n+1}_{\mathrm{L},i-1,j}}{\Delta x}\right]$$

$$+ \frac{1}{Le\,Pr}\Delta x\left[D_{i,j+(1/2)}\frac{C^{n+1}_{\mathrm{L},i,j+1} - C^{n+1}_{\mathrm{L},i,j}}{\Delta y}\right.$$

$$\left. - D_{i,j-(1/2)}\frac{C^{n+1}_{\mathrm{L},i,j} - C^{n+1}_{\mathrm{L},i,j-1}}{\Delta y}\right]. \tag{23}$$

The following assumptions have been made in arriving at this equation:

(1) The densities of the liquid and solid phases are constant and equal, so that a simple mixture rule applies, i.e.,

$$C_{\mathrm{mix}} = C_{\mathrm{S}} f_{\mathrm{S}} + C_{\mathrm{L}} f_{\mathrm{L}}. \tag{24}$$

(2) There is no diffusion in the solid (except in the cells that contain the interface, in which the equilibrium lever rule is assumed); the concentration at which the solute first solidifies is the concentration at which that portion of solid remains for all time t.

Solution of this finite difference equation requires a model for the phase transformation thermodynamics at the solidification front. Figure 4 shows a portion of the linearized Sn–Bi binary alloy equilibrium phase diagram [20]. The important parameters are the partition or distribution coefficient, K and the slope of the liquidus line, m. For the purposes of our model, we assume that $T_{\mathrm{L}} \approx T_{\mathrm{S}} \approx T_{\mathrm{M}}$ for all concentrations encountered; thus, there is no effect of concentration on melting temperature and the liquid/solid interface remains distinct like that for a pure material. The significant result of this assumption is that the enthalpy method, as described in Section 3.2, is decoupled from the concentration equation and is the only mechanism necessary to determine the location of the solidification front.

The foregoing assumptions and thermodynamic relations allow us to express the rate of accumulation of solute in an infinitesimal control volume in terms of the liquid concentration and the solid (or liquid) fraction [9]

$$\frac{\partial C_{\mathrm{mix}}}{\partial t} = KC_{\mathrm{L}}\frac{\partial f_{\mathrm{S}}}{\partial t} + \frac{\partial}{\partial t}(f_{\mathrm{L}} C_{\mathrm{L}}). \tag{25}$$

Thus, the *LHS* of the discretized equation for solute concentration becomes

$$\frac{[C^{n+1}_{\mathrm{mix}i,j} - C^{n}_{\mathrm{mix}i,j}]\,\Delta x\,\Delta y}{\Delta t} = \frac{[f^{n}_{\mathrm{L}} C^{n+1}_{\mathrm{L}} - \alpha^{n}_{i,j} C^{n}_{\mathrm{L}}]\,\Delta x\,\Delta y}{\Delta t} \tag{26}$$

in which

$$\alpha^{n}_{i,j} = [(K-1)f^{n+1}_{\mathrm{L}} + (2-K)f^{n}_{\mathrm{L}}]$$

and this is known at time step n since the liquid fractions at $n+1$ are recovered directly from the solution of the energy equation (as outlined in Section 3.2). The solute concentration in the solid portion of a node may be found from employing the relation

$$C^{n+1}_{\mathrm{S}} = \frac{C^{n}_{\mathrm{S}} f^{n}_{\mathrm{S}} + KC^{n}_{\mathrm{L}}(f^{n+1}_{\mathrm{L}} - f^{n}_{\mathrm{L}})}{f^{n+1}_{\mathrm{S}}}. \tag{27}$$

Note the elegance of this new formulation: in a completely solid node for the time interval $[n, n+1]$, no computation is required, since the diffusion coefficient for the solid material is zero. For a fully liquid node over $[n, n+1]$, $f_{\mathrm{L}} = 1$ and it can be readily seen that the equation reduces to the simple case of solute transfer for C_{L} in the absence of phase change. In nodes which contain both solid and liquid over $[n, n+1]$ the general formulation holds; the liquid concentration is the working variable in the discretized equation (26) and the solid concentration is recovered from equation (27).

The discretized equation (26) is solved by Gauss–Seidel iteration in a manner analogous to the energy equation, i.e.,

$$[\alpha^{p}_{ij} + \Lambda^{p}_{ij}]C^{p+1}_{\mathrm{L},ij} = rhs^{p}_{ij}. \tag{28}$$

The solution scheme for solidification in a two-dimensional cavity subject to thermosolutal convection has now been fully specified.

3.4. *Grid independence study*

A comprehensive grid independence study was undertaken to determine the appropriate spatial discretization, temporal discretization and iteration convergence criterion to be used. This study involved evaluating the solution fields of a test matrix of simulations at four different mesh spacings (Table 1) and

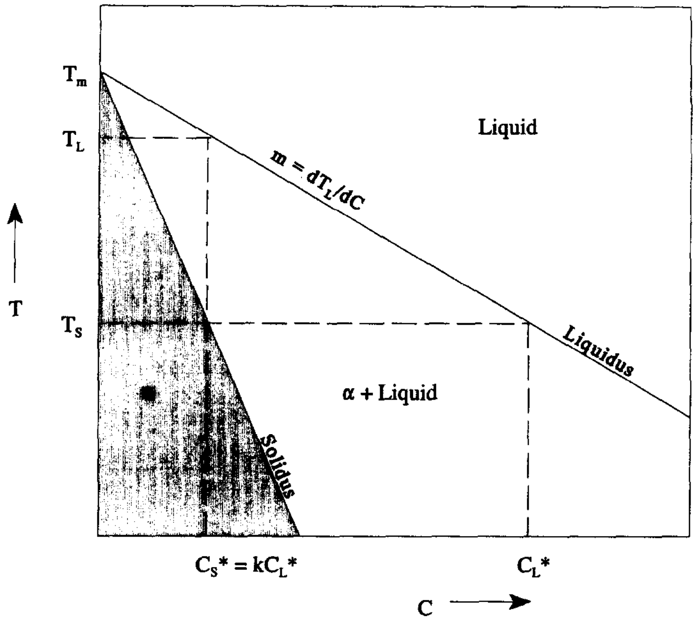

Fig. 4. Linearized equilibrium phase diagram for a binary alloy system.

Table 1. Effect of grid size on the results ($\Delta t = 6.250 \times 10^{-6}$; $\varepsilon = 10^{-6}$)

Grid	h	$\psi_{\min}$	$\|u_{\max}\|$	$\|v_{\max}\|$	θ_{mid}	x_f
500 time steps						
21 × 16	0.04	−0.1281	0.5697	0.4587	0.8656	0.8911
		(0.55, 0.4)	(0.5, 0.05)†	(0.05, 0.4)		
		68%	70%†	37%	1.6%	2.0%
41 × 31	0.02	−0.07608	0.3357	0.3358	0.8795	0.8733
		(0.375, 0.4)	(0.375, 0.65)	(0.075, 0.4)		
		6.2%	9.9%	3.6%	0.1%	0.4%
61 × 46	0.02	−0.08115	0.3727	0.3483	0.8805	0.8698
		(0.4167, 0.4)	(0.4167, 0.65)	(0.0833, 0.41167)		
		1.38%	**2.0%†**	**1.8%**	**0.07%**	**0.2%**
81 × 61	0.01	−0.08229	0.3803	0.3545	0.8811	0.8681
		(0.425, 0.4)	(0.4375, 0.0625)†	(0.075, 0.4)		
20 000 time steps						
21 × 16	0	−0.03305	0.2288	0.2475	0.4632	0.3440
		(0.3, 0.6)	(0.25, 0.55)	(0.05, 0.3)		
		44%	40%	40%	17%	16%
41 × 31	0	−0.05937	0.3874	0.4092	0.5621	0.4116
		(0.225, 0.55)	(0.1, 0.55)	(0.025, 0.425)		
		8.2%	11%	4.0%	2.3%	2.2%
61 × 46	0	−0.06465	0.4262	0.4336	0.5854	0.4210
		(0.233, 0.5167)	(0.2333, 0.3833)	(0.0883, 0.5167)		
		5.3%	**1.9%**	**5.6%**	**2.6%**	**0.9%**
81 × 61	0	−0.0683	0.4344	0.4594	0.6009	0.425
		(0.425, 0.4)	(0.2375, 0.3625)	(0.075, 0.5125)		

† For the 21 × 16 and 81 × 61 grids, the maximum horizontal velocity was negative and at the bottom of the cavity, for the 41 × 31 and 61 × 46 grids, the maximum horizontal velocity was positive and at the top of the cavity.

five time-step sizes (Table 2) at two different finish times, as well as four different iteration tolerances (Table 3). The quantities examined were:

- $\psi_{\min}$, the minimum value of vector potential, and its location;
- $|u_{\max}|$, the maximum magnitude of the horizontal velocity component, and its location;
- $|v_{\max}|$, the maximum magnitude of the vertical velocity component, and its location;
- θ_{mid}, the value of nondimensional temperature at the midpoint of the solution domain (0.5, 0.375);

Table 2. Effect of time-step size on the results (61 × 46 mesh ; $\varepsilon = 10^{-6}$)

Δt (steps)	$\psi_{\min}$	$\lvert u_{\max}\rvert$	$\lvert v_{\max}\rvert$	θ_{mid}	x_f
Nondimensional finish time = 0.03375					
6.25×10^{-5}	−0.09705	0.5169	0.4798	0.7855	0.6295
(500)	(0.3, 0.475)	(0.325, 0.65)	(0.1, 0.475)		
	0.7%	0.0%†	2.4%	0.3%	0.1%
3.125×10^{-5}	−0.09774	0.5170†	0.4916	0.7878	0.6303
(1000)		(0.325, 0.675)			
	0.2%	0.0%†	0.2%	0.0%	0.0%
1.25×10^{-5}	−0.09797	0.5169	0.4927	0.7880	0.6306
(2500)	0.1%	0.1%	0.1%	0.0%	0.0%
0.625×10^{-5}	−0.09805	0.5172	0.4931	0.7880	0.6305
(5000)	0.0%	0.0%	0.0%	0.0%	0.0%
0.3125×10^{-5}	−0.09807	0.5173	0.4933	0.7879	0.6303
(10 000)					
Nondimensional finish time = 0.0135					
6.25×10^{-5}	−0.05937	0.3877	0.4089	0.5609	0.4114
(2000)	(0.225, 0.55)	(0.1, 0.55)	(0.25, 0.425)		
	0.0%	0.1%	1.0%	0.5%	0.3%
3.125×10^{-5}	−0.05936	0.3872	0.4129	0.5637	0.4127
(4000)	0.1%	0.0%	0.2%	0.1%	0.1%
1.25×10^{-5}	−0.05932	0.3871	0.4136	0.5634	0.4122
(10 000)	0.1%	0.1%	1.0%	0.2%	0.1%
0.625×10^{-5}	−0.05937	0.3874	0.4092	0.5621	0.4116
(20 000)					
0.3125×10^{-5}	not necessary				
(40 000)					

† The maximum horizontal velocity was positive and at the top of the cavity.

Table 3. Effect of tolerance level on the Gauss–Seidel solution scheme results ($\Delta t = 6.250\times10^{-6}$)

ε	$\psi_{\min}$	$\lvert u_{\max}\rvert$	$\lvert v_{\max}\rvert$	θ_{mid}	CPU
500 time steps					
10^{-4}	−0.1028	0.4561	0.3784	0.9060	190
	(0.45, 0.3667)	(0.4833, 0.0667)	(0.7833, 0.3167)		
	4.8%	0.5%	1.6%	1.8%	
10^{-5}	−0.09809	0.4539	0.3846	0.8896	186
	(0.45, 0.3667)	(0.4067, 0.0833)	(0.7833, 0.3167)		
	2.9%	1.3%	0.7%	1.1%	
$\mathbf{10^{-6}}$	**−0.09535**	**0.4481**	**0.3819**	**0.8796**	**191**
	(0.45, 0.3667)	**(0.45, 0.0833)**	**(0.7833, 0.3167)**		
	0.2%	**0.3%**	**0.1%**	**0.3%**	
10^{-7}	−0.09513	0.4467	0.3816	0.8769	198
	(0.45, 0.0833)	(0.45, 0.0833)	(0.7833, 0.3167)		

- x_f, the average value of the front location.

In the tables, the percentages quoted are a comparison with the result at the next level of mesh refinement.

The results indicated that a spatial discretization of 61 × 46 mesh points (grid size $h = 0.01667$), a time step of $\Delta t = 1.25\times10^{-5}$ and a Gauss–Seidel iteration tolerance of $\varepsilon = 10^{-6}$ were the appropriate values to employ to furnish an accurate solution without performing unnecessary calculations. The maximum change in the variables examined between the 61 × 46 mesh and the next level of mesh refinement tested (81 × 61 points) was 5.6%. The maximum change between the selected Δt and the next smallest time step tested ($\Delta t = 0.625\times10^{-5}$) was 1.0%, and the maximum change between the selected iteration tolerance of $\varepsilon = 10^{-6}$ and a tolerance $\varepsilon = 10^{-7}$ was 0.3%. The thermal field changes most rapidly at the beginning of the simulation when transients are at their highest. Correspondingly, it was observed during the test simulations for determining the spatial grid size that $O(100)$ iterations are required initially, while $O(1)$ iteration is required later on, once the initial transients decrease. For this reason, simulations in Table 3 were performed to the one early finish time of 500 time steps.

With regard to the selection of an appropriate time step, it appears from Table 2 that even the largest time step tested (6.25×10^{-5}) is suitable; however it was noted that the use of this time step and the next smaller time step (3.125×10^{-5}) led to the algorithm failing to capture the front during the very first few time steps (where transients are at a maximum). This led to the selection of 1.25×10^{-5} as the appropriate time step for the simulations carried out in this paper. A scheme which dynamically evaluates the characteristic velocity and temperature scales and selects an appropriate time step at each cycle subject to limits on the truncation error caused is under development and should lead to a further reduction in the CPU burden involved in obtaining a solution.

4. RESULTS AND DISCUSSION

4.1. *Directional solidification of pure tin*

Simulations for the solidification of pure tin in a differentially heated cavity with an aspect ratio of 0.75 were performed. The important physical parameters for this case are $L = 8.89$ cm, $Ra = 1.4 \times 10^5$, $Pr = 0.017$, $T_H = 233°C$, $T_C = 229°C$, $\Delta H = 59 \times 10^3$ J kg^{-1} K^{-1}, and $C_p = 255$ J kg^{-1} K^{-1}. Thermophysical properties for the liquid phase are considered to be constant and equal to those in the solid phase. A 61×46 mesh was used. The physical parameters correspond to the experiments and simulations in [4]. Other researchers [5, 6] have also performed simulations for this case.

The isotherms and velocity vectors at time $t = 0.165$ h for this simulation are shown in Fig. 5. By this time, the solidification front has propagated from the chilled wall through the cavity under the action of both conductive and convective heat transfer. The isotherms in the solid region are typical of conduction in a solid; the temperature gradient is very steep as a result of pure conduction. The isotherms become vertical as they approach the cold wall. In the liquid domain, the isotherms exhibit a distinct reverse 's' shaped distortion, which is characteristic of buoyancy-driven natural convection at a high Rayleigh number [21]. The isotherms compare well with the numerical results of Raw and Lee [5]. The velocity vectors indicate that a strong convective cell has developed with almost quiescent fluid at the four corners of the liquid domain. Hot fluid rises at the hot wall and flows along the top of the cell toward the solidification front, where it is cooled and falls to the lower surface under the action of gravity, circulating once again to the foot of the hot wall. This continual convection of warm fluid to the uppermost segment of the solidification front delays its propagation along the cavity. As a result the solidification front is distorted into an 's'-shape like the fluid isotherms. In the

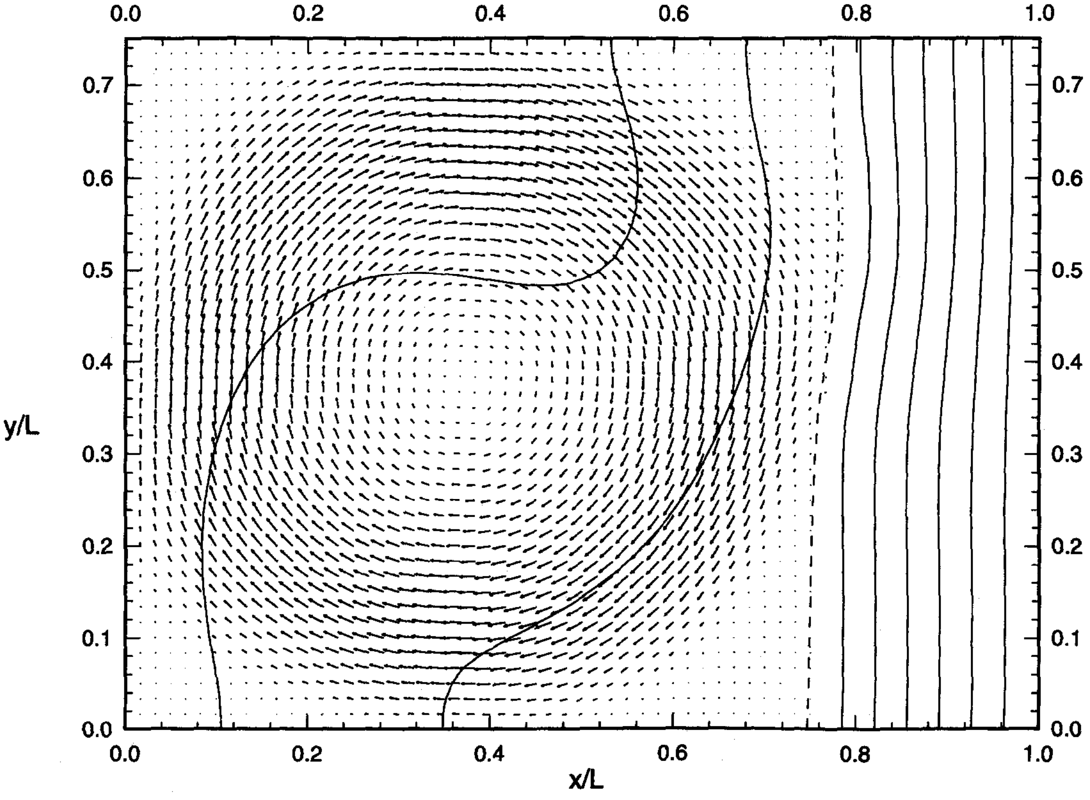

Fig. 5. Velocity vectors and isotherms at $t = 0.165$ h. Isotherms are at intervals of $\Delta\theta = 0.1$. Dashed line is the front location.

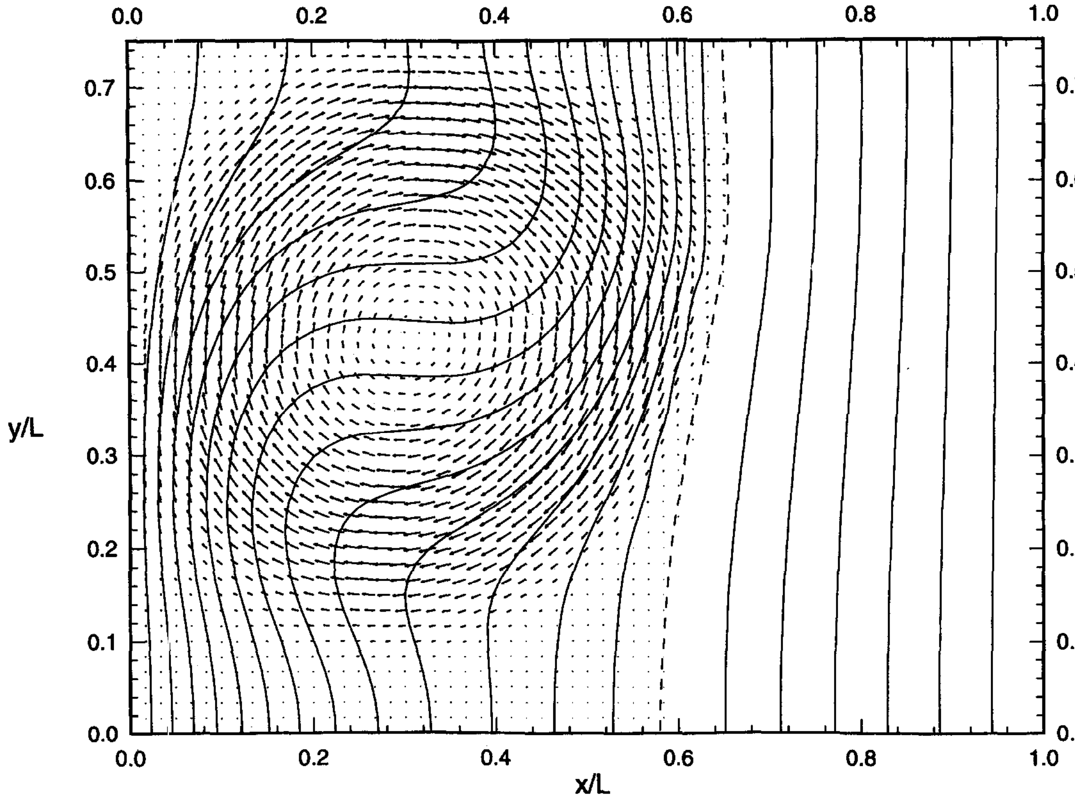

Fig. 6. Velocity vectors and isotherms at $t = 0.569$ h. Isotherms in the melt are at the increased resolution of $\Delta\theta = 0.02$.

absence of buoyancy-induced natural convection the solidification front would have been vertical [22].

The minimum value of the nondimensional stream function for the results in Fig. 5 was found to be $\psi_{\min} = -0.1159$. The corresponding value found by Raw and Lee [5] was -0.1295. The streamlines also compare well with the numerical results of Raw and Lee. The stronger convection predicted by their simulation may be due to the higher Grashof number resulting from their selection of different reference properties for tin, and their use of variable properties. It must be noted that significant differences exist between material properties listed in different sources in the literature; in the present work, the properties listed in Yao *et al.* [23] were used.

Figure 6 shows velocity vectors and isotherms at a later time in the simulation, $t = 0.529$ h. Extra isotherms are shown to permit easier comparison to the numerical results of Zhang *et al.* [6]. The numerical results are generally in good agreement. Our results indicate lower-strength convection at this time. In particular, we predict a region of low-velocity fluid at the bottom of the melt which does not take part in the main convective recirculation. A possible explanation for this is a difference in fluid properties used in the two simulations. The predicted front locations appear to be similar in shape for both simulations.

Results further into the solidification process are shown in Fig. 7 for time $t = 1.896$ h. The solidification front has propagated much further into the melt, with over half of the cavity being comprised of solid tin. The velocity vectors show that two convective cells have formed at this time. The primary recirculating zone at the top of the cell remains similar to the $t = 0.165$ h case. A single convection cell could not be sustained in the presence of the sloping interface and weaker natural convection (due to the locally decreased melt size). Thus the lower cell forms, circulating in the same direction as the primary cell and entraining cold recirculating fluid from the primary cell. A similar convective pattern is indicated in the results of Dantzig [24] for the simulation of the melting of pure gallium when the melt region is of a similar shape. The results of Raw and Lee [5] indicate stronger convection, with $\psi_{\min} = -0.07887$ compared to our value of -0.06329. In addition they did not indicate a breakdown to a dual-cell convective pattern at this time. To investigate this discrepancy, the values of potential in the lower convective cell from our results were examined. Raw and Lee predict roughly $\psi = -0.016$ compared with our value of -0.0119. This comparison indicates that the difference between the two sets of results is not as dramatic as might be inferred from the appearance of the convection vectors. The difference is merely that our simulation predicts a lower value of potential in the lower portion

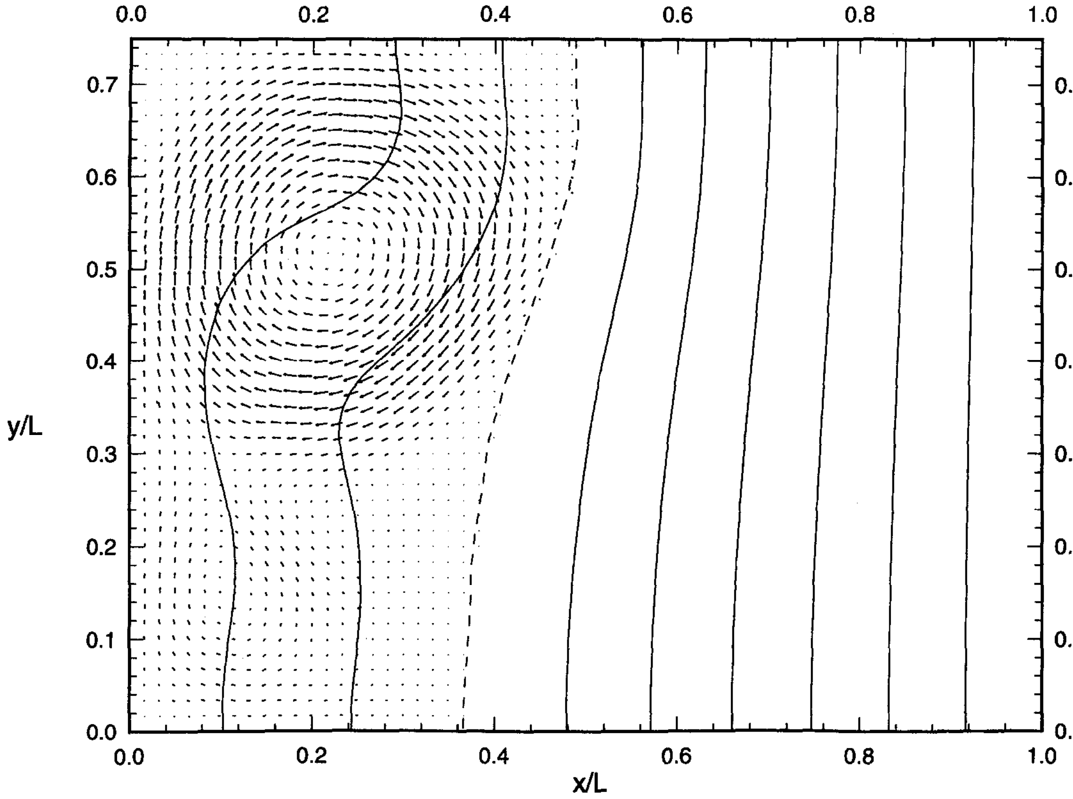

Fig. 7. Velocity vectors and isotherms at $t = 1.896$ h.

of the cavity, leading to the mild secondary circulation, compared to the stronger convection at this location predicted by Raw and Lee [5].

The predicted solidification front locations from the present study are compared to experimental data [4] and numerical predictions in the literature [5, 6] in Fig. 8. The current predictions are in acceptable agreement with the experimental results. At times $t = 0.077$ h and $t = 0.165$ h, the solidification front has propagated quite rapidly, controlled primarily by the action of conduction at the chilled wall. Some convective effects are in play since the front is not vertical. The predicted front location from the numerical analysis at these early times is further advanced than the experimental results. At a time $t = 0.077$ h the mid-point of the front is 15% further advanced than the experimental value, and at time $t = 0.165$ h this value is 6%. This discrepancy in front location may be explained by the observations of Wolff and Viskanta on the thermal inertia of the experimental apparatus. The apparatus was not capable of producing an instantaneous temperature drop to T_C at the cold wall at time $t = 0$; rather 0.033 h elapsed before the cold plate temperature reached T_C. At the later times, the predicted front location tends to lag behind the experimentally determined location. Also, the numerical results fail to predict the increased thickness of the front at the bottom of the cavity. Both of these discrepancies may be attributed to the imperfect insulating material at the bottom of the experimental apparatus [4]. The numerical results in [5, 6] exhibit similar discrepancies when compared to the experiments.

The predicted temperature values along three different cavity heights are shown in Fig. 9 at time $t = 0.077$ h. Corresponding experimental values from [4] and predictions from [5] are also shown. The curves for $y/H = 0.9$ and $y/H = 0.5$ indicate reasonable agreement with the experimental data. The curves depart from the experimental data for larger values of x/L, with the experimental values being 45% larger at a x/L value of 0.76 but contained within 15% in the range $0 \leqslant x/L \leqslant 0.70$. Again, thermal inertia of the test apparatus is a possible cause of this discrepancy. The curve for $y/H = 0.1$ is significantly different from the experimental results, with the numerical values being up to 100% larger than the experimental values over the range $0 \leqslant x/L \leqslant 0.8$. Once again, it seems very likely that the source of this error is the effect of the imperfect insulation on the bottom of the experimental apparatus. In addition, Wolff and Viskanta also noted that their temperature measurements were subject to scatter. The curves for $y/H = 0.5$ and 0.9 exhibit superior agreement to the experimental data than those of Raw and Lee [5] while the $y/H = 0.1$ curve deviates further.

The CPU requirement for this simulation was

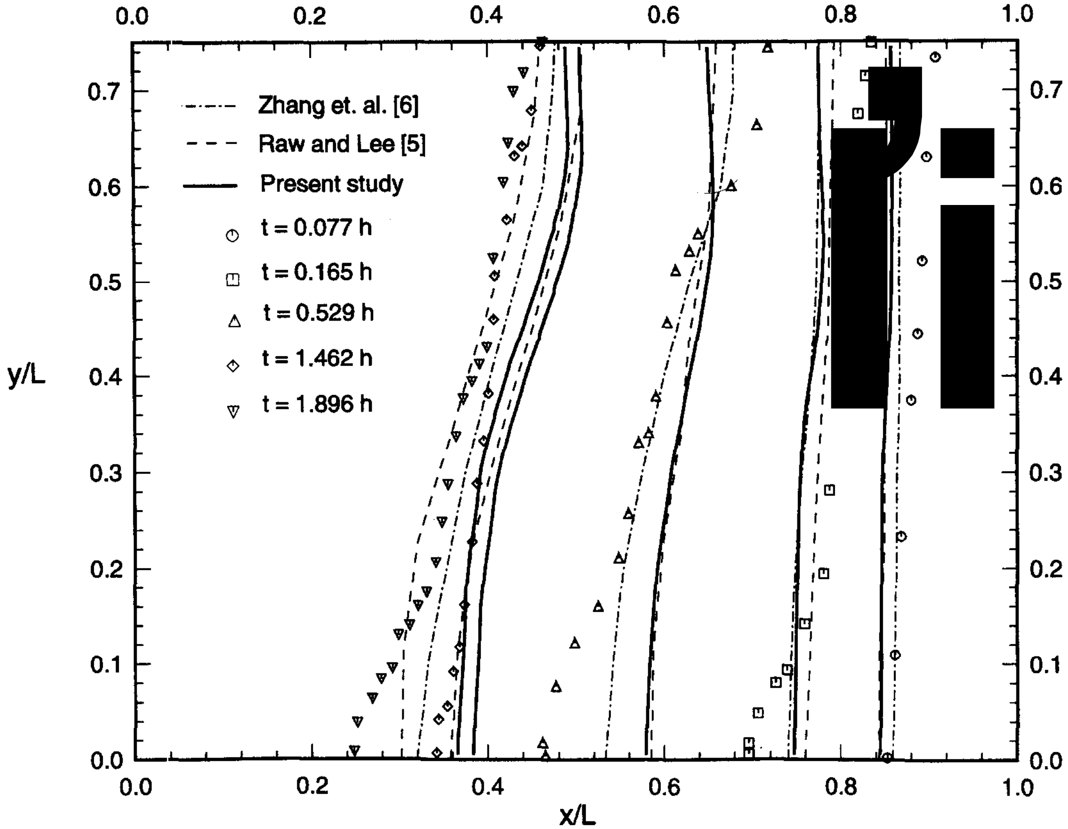

Fig. 8. Comparison of experimentally determined [4] and numerically predicted front locations (present study and [5, 6]) at various times. Note that no front locations are provided in [6] for the $t = 1.896$ h case.

approximately 3.5 h on a DEC 3000/700 (225 MHZ, SPECfp95 5.71) for a mesh of 61 × 46. This compares with the two-domain approach [6] which required 45 h on a SUN Sparc 10 workstation for a transforming mesh of 42 × 42 points, and with that of Raw and Lee [5] which required 0.73 h on a CDC Cyber 840 supercomputer for a single-domain solution with a fixed mesh of 41 × 31 points.

4.2. *Simulation of Sn–Bi alloy solidification*

Simulations for the solidification of a Sn–Bi binary alloy system were performed. In order to effect a tractable buoyancy ratio, the dimensions of the solution domain and the temperature difference were altered from the case of pure tin above to: $L = 5$ cm, $T_C = 217.9°C$, $T_H = 237.9°C$. The initial solute concentration was 0.5%Bi; in addition, $Le = 4.0 \times 10^3$, $K = 0.36$, $R_B = 5.05$. Thermophysical properties used were as those for the pure tin case, and the cavity aspect ratio was maintained at 0.75. An additional simulation was performed for the pure tin case using the new temperature difference and cavity dimensions to provide a basis for comparison for the alloy results. The CPU time required for 10 000 time steps (real time $t = 0.621$ h) was 1.2 h. To assess the ability of the solution scheme to conserve solute, the total amount of solute present in the system (solid + liquid) was examined at each time step. It was found that the total mass of the solute increased as the solution proceeded. The maximum value found, after 10 000 time steps, was 4% larger than the initial total mass of the solute. The reason for this discrepancy is the errors introduced in the discretization of equation (25).

The isotherms and velocity vectors for this alloy solidification problem are shown in Fig. 10 at $t = 0.062$ h. The results are similar in character to those found for pure tin. However, the strength of convection is smaller than that at the corresponding time for pure tin ($\psi_{\min} = -0.1109$ as opposed to -0.1111). Since bismuth has a higher density than tin, once the solute has been distributed throughout the flow field by thermal convection, it will act to oppose that convection and hence retard the action of the thermal convective cell.

Figure 11 shows lines of constant solute concentration in the fluid at this same time (0.062 h). The solute concentration field in Fig. 11 corresponds well to the results shown in Fig. 10. As can be readily seen, solute is rejected at the interface, since the solid forms at a lower concentration than the liquid with which it is in contact. This rejected solute descends under the

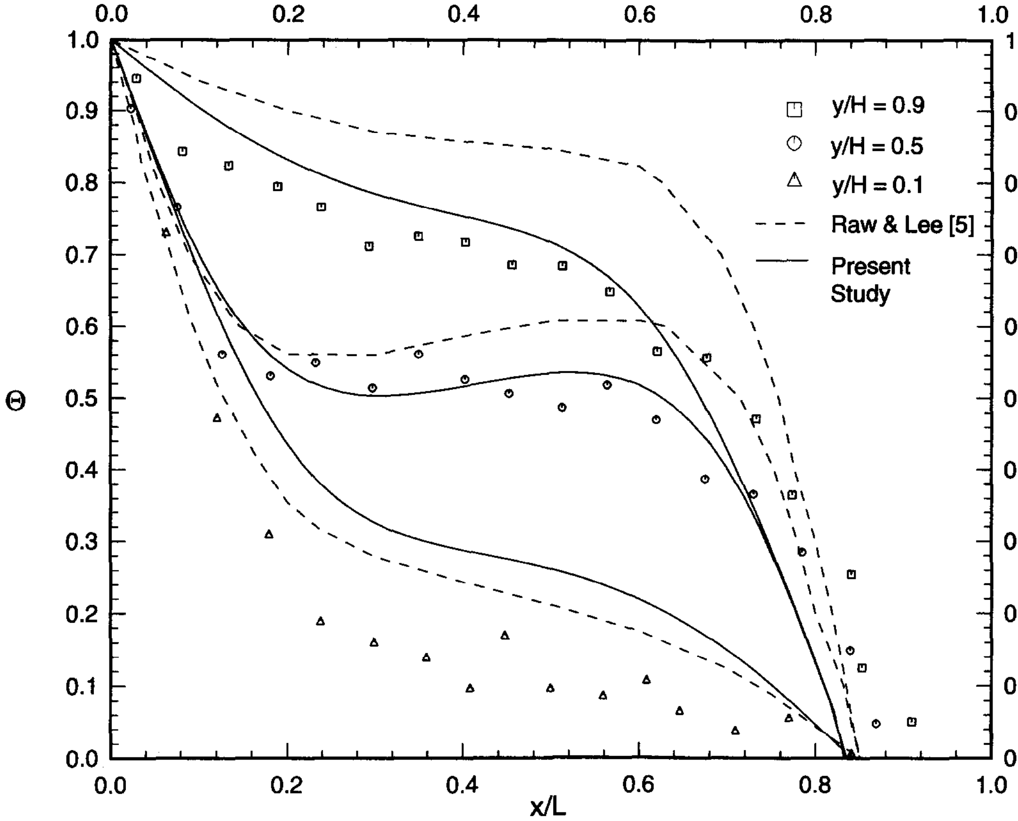

Fig. 9. Comparison of experimentally determined [4] and numerically predicted temperatures (present study and [5]) in the melt region.

action of gravity to the bottom of the cavity, from where it is redistributed throughout the domain by the thermally-driven convective cell. Also, the mean concentration of solute in the melt increases with time. Near the top of the interface is a solute-deficient region of fluid. The concentration gradients agree qualitatively with those of Thompson and Szekely [25] as well as with low-Prandtl number fluid results [10].

Figure 12 shows the isotherms and velocity vectors at a later time, $t = 0.6207$ h. The results are again similar in character to those found for pure tin. The convection in the primary recirculation is weaker than for the pure tin case ($\psi_{\min} = -0.06485$ rather than -0.06494). Interestingly, the secondary recirculation exhibits higher convection ($\psi_{\min} = -0.01432$ rather than -0.01424).

Figure 13 is a plot of lines of constant solute concentration in the melt. The average concentration in the bulk of the melt has risen to approximately 0.72% from the initial value of 0.5% as the front has propagated into the melt, rejecting solute rich fluid at the interface which is then convected throughout the melt. The lines of constant solute concentration clearly indicate the influence of the convection patterns on the distribution of the solute.

Figure 14 shows a comparison of the front locations for pure tin and for the Sn–Bi alloy system at several times. The solidification front locations for the alloy system have propagated slightly further into the melt, particularly in the top section of the domain which is subject to higher levels of convective heat transfer. This can be explained by the slightly weaker convection cell which forms. At the earlier times, the front locations agree more closely; the solute gradients at this time have not established themselves to oppose the thermal driving force. It is interesting to note that the general shape of the interface retains its 's' shaped characteristic in the alloy system.

5. CONCLUSIONS

A fixed-grid method has been formulated for the efficient solution of convection–conduction phase change problems involving pure materials and simple binary alloys. The enthalpy method is used to model the propagation of the solidification front and to solve for the temperatures throughout the entire domain. A direct solver is employed for the solution of the velocity field. Solute concentrations are found using a simplified model of binary alloy solidification similar to the enthalpy method. Simulations (at a high Rayleigh number and low Prandtl number) for the direc-

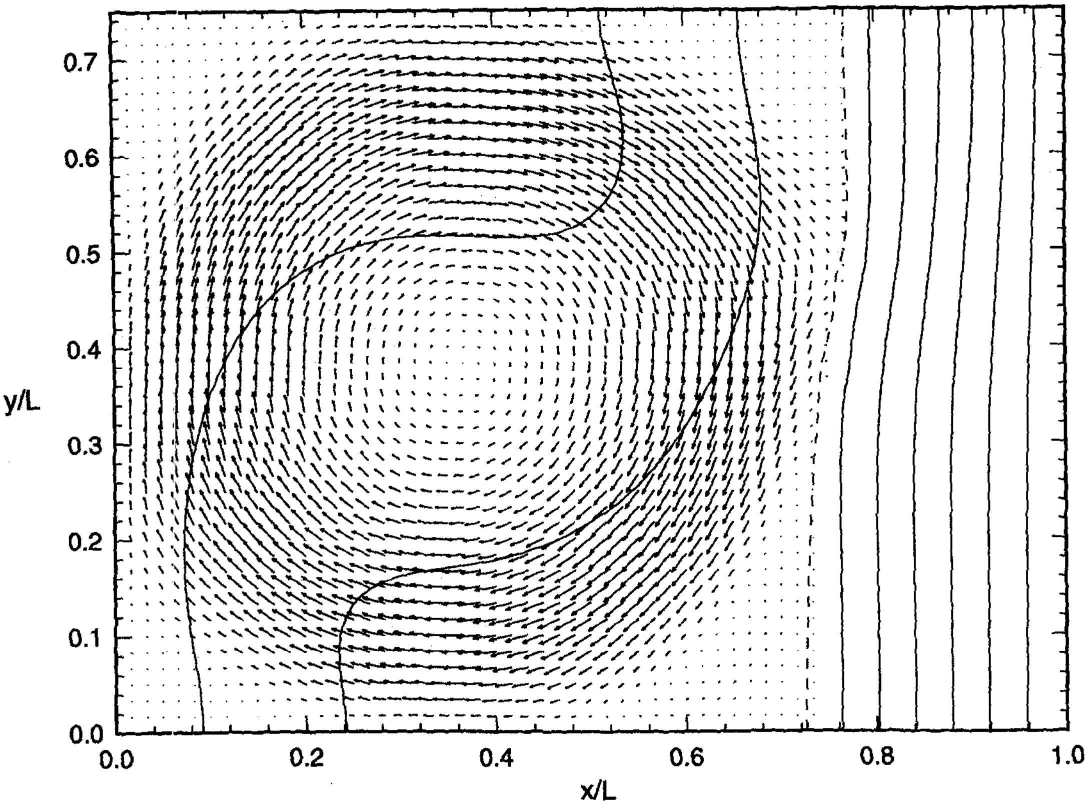

Fig. 10. Velocity vectors and isotherms for Sn–0.5%Bi at t = 0.062 h. Isotherms are at intervals of $\Delta\theta = 0.1$. Dashed lines in the front location.

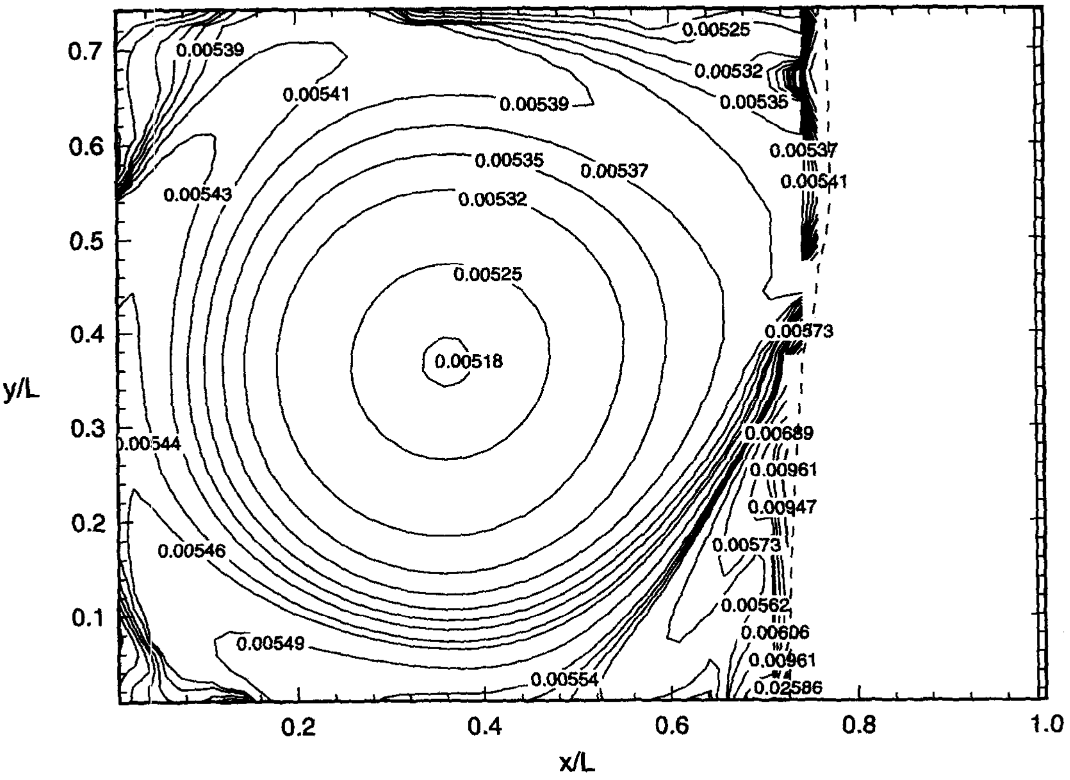

Fig. 11. Lines of constant bismuth concentration in the melt region at t = 0.062 h.

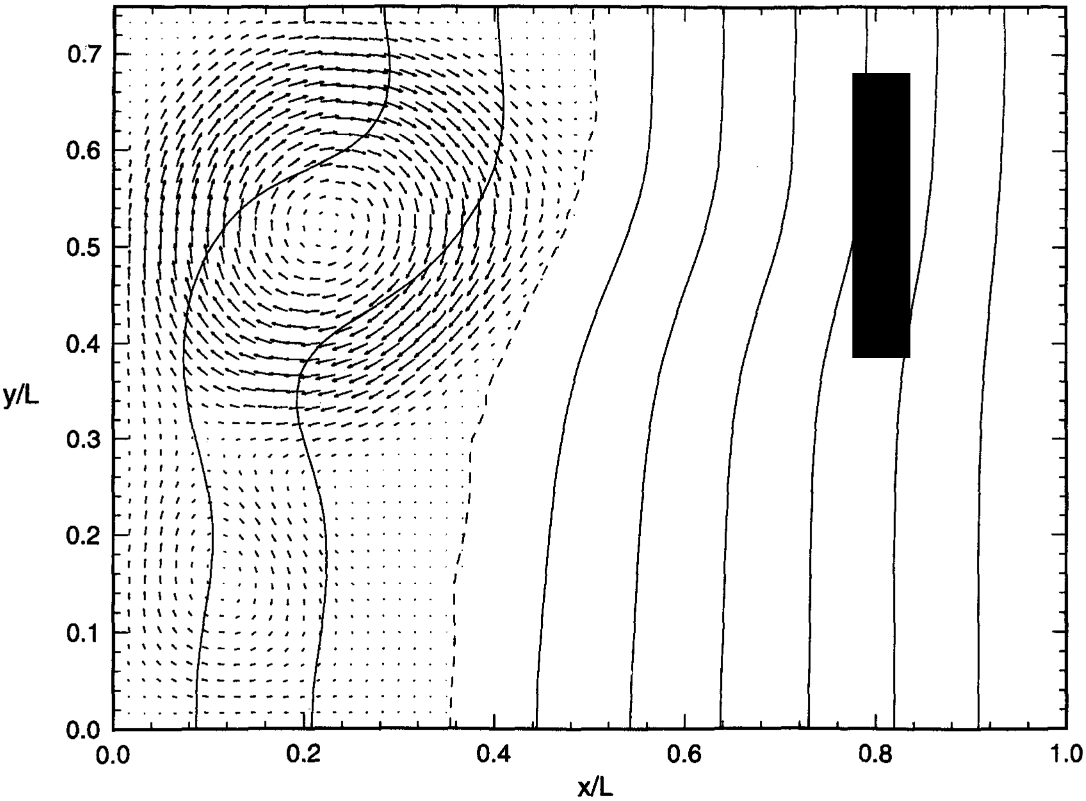

Fig. 12. Velocity vectors and isotherms for Sn–0.5%Bi at $t = 0.621$ h. Isotherms are at intervals of $\Delta\theta = 0.1$. Dashed line is the front location.

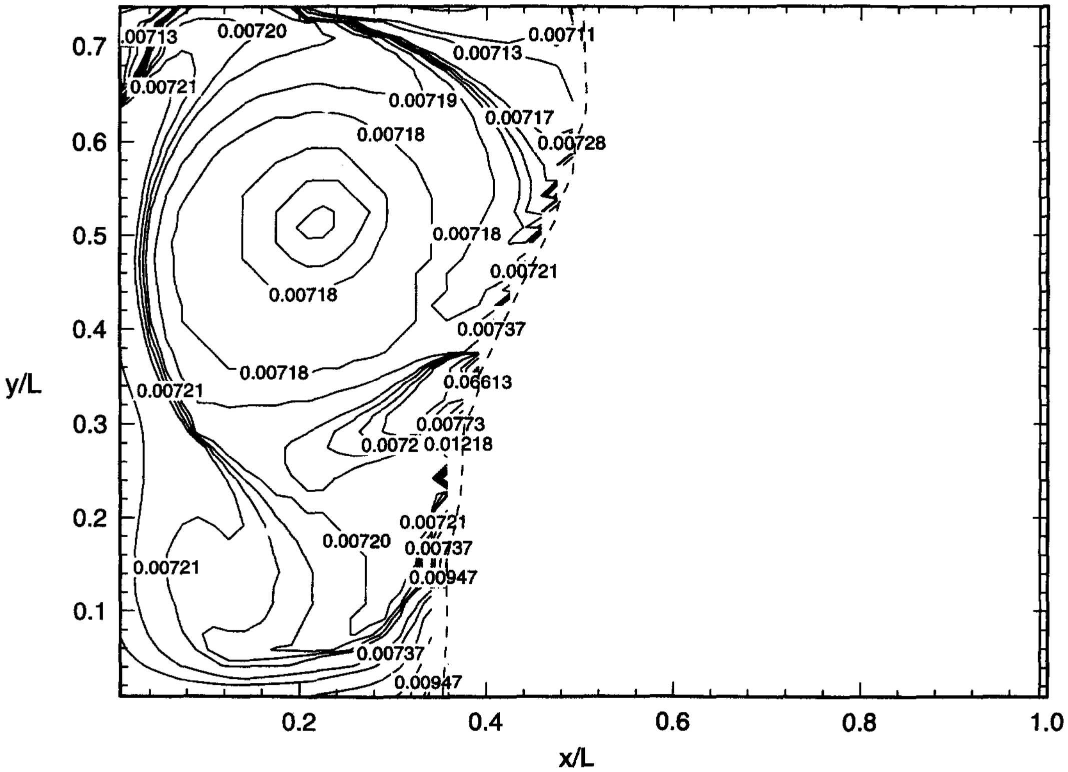

Fig. 13. Lines of constant bismuth concentration in the melt region at $t = 0.621$ h.

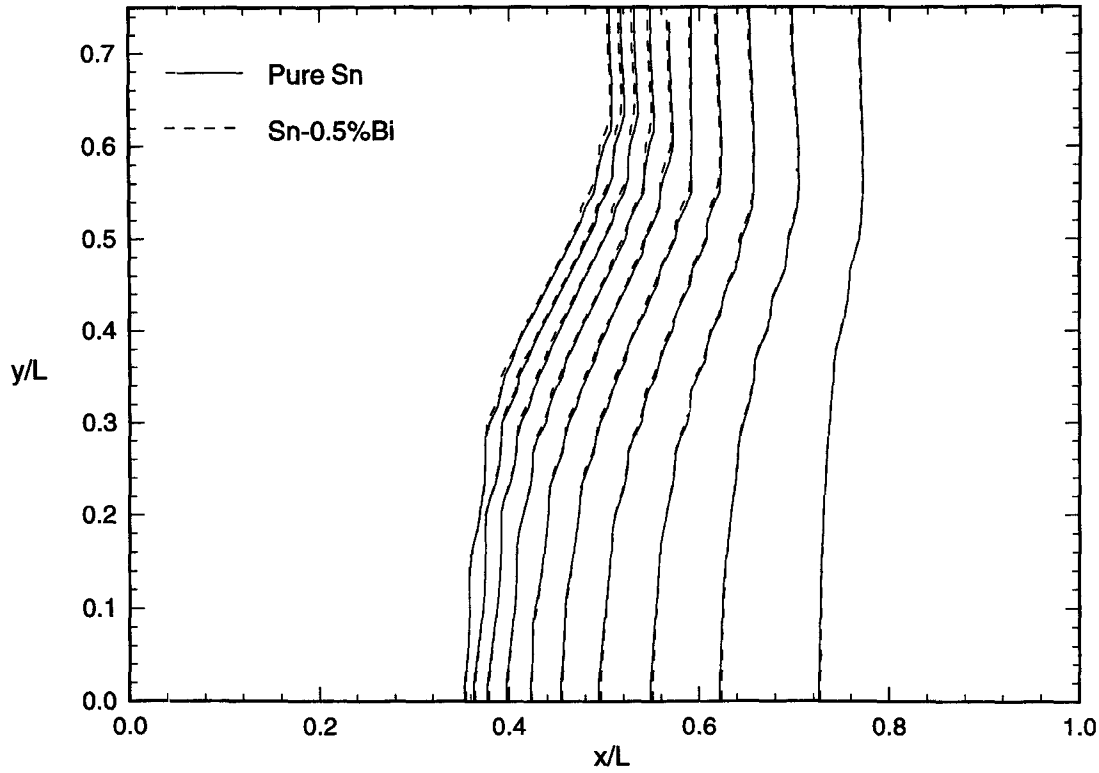

Fig. 14. Comparison of numerical predictions for front location as the material solidifies. Lines are at time intervals of 1000 time steps or 0.062 h.

tional solidification of pure tin were performed. The results were found to agree well with experimental data [4] and with numerical solutions [5, 6]. Results for the solidification of a Sn–0.5%Bi alloy were also presented and discussed.

Acknowledgements—Partial support for this work from the National Science Foundation (Grant CTS-9210612) is gratefully acknowledged. J.E.S. was funded by a fellowship from the University of Wisconsin-Milwaukee. Professors G. de Vahl Davis and E. Leonardi, and Dr V. Timchenko, of the University of New South Wales are particularly thanked for kindly providing their code, FRECON3V, which was the starting point for this work.

REFERENCES

1. Zeng, X. and Faghri, A., Temperature-transforming model for binary solid–liquid phase-change problems. Part I: Mathematical modeling and numerical methodology. *Numerical Heat Transfer*, 1994, **25B**, 467–480.
2. Zeng, X. and Faghri, A., Temperature-transforming model for binary solid–liquid phase-change problems. Part II: Numerical simulation. *Numerical Heat Transfer*, 1994, **25B**, 481–500.
3. Garimella, S. V., McNulty, J. P. and Schlitz, L. Z., Formation and suppression of channels during upward solidification of a binary mixture. *Metall. and Mater. Trans.*, 1995, **26A**, 971–981.
4. Wolff, F. and Viskanta, R., Solidification of a pure metal at a vertical wall in the presence of liquid superheat. *International Journal of Heat and Mass Transfer*, 1988, **31**, 1735–1744.
5. Raw, W. Y. and Lee, S. L., Application of weighting function scheme on convection–conduction phase change problems. *International Journal of Heat and Mass Transfer*, 1991, **34**, 1503–1513.
6. Zhang, H., Prasad, V. and Moallemi, M. K., Numerical algorithm using multizone adaptive grid generation for multiphase transport processes with moving and free boundaries. *Numerical Heat Transfer*, 1996, **29B**, 399–421.
7. Bennon, W. D. and Incropera, F. P., A continuum model for momentum, heat and species transport in binary solid–liquid phase change systems—I. Model formulation. *International Journal of Heat and Mass Transfer*, 1987, **30**, 2161–2170.
8. Viskanta, R. and Beckerman, C., Mathematical modeling of solidification. *Proceedings of the Symposium on Interdisciplinary Issues in Materials Processing and Manufacturing*. Boston, MA, 1987.
9. Voller, V. R., Brent, A. D. and Prakash, C., The modelling of heat, mass and solute transport in solidification systems. *International Journal of Heat and Mass Transfer*, 1989, **32**, 1719–1731.
10. Hyun, M. T., Kuo, D. C., Bergman, T. L. and Ball, K. S., Direct simulation of double diffusion in low Prandtl number liquids. *Numerical Heat Transfer*, 1995, **27A**, 639–650.
11. Mallinson, G. D. and de Vahl Davis, G., Three-dimensional natural convection in a box: a numerical study. *Journal of Fluid Mechanics*, 1977, **83**, 1–31.
12. Mallinson, G. D. and de Vahl Davis, G., The method of the false transient for the solution of coupled elliptic equations. *Journal of Computational Physics*, 1973, **12**, 435–461.
13. Alexiades, V. and Solomon, A. D., *Mathematical*

Modeling of Melting and Freezing Processes. Hemisphere, Washington D.C., 1993.

14. Simpson, J. E. and Garimella, S. V., Melt convection and front propagation in the unidirectional solidification of a pure material. *Proceedings of the 4th Decennial International Conference on Solidification Processing*, ed. J. Beech and H. Jones. Sheffield, U.K., July 1997, pp. 130–134.
15. Timchenko, V., Leonardi, E. and de Vahl Davis, G., FRECON3V User's Manual (Report 1997/FMT/1) and Programmer's Manual (Report 1997/FMT/2), University of New South Wales, School of Mechanics and Manufacturing Engineering, 1997.
16. Samarskii, A. A. and Andreyev, V. B., On a high-accuracy difference scheme for an elliptic equation with a several space variables. *USSR Comput. Math. and Math. Phys.*, 1963, **3,** 1373–1382.
17. Voller, V. R., Markatos, N. and Cross, M., Techniques for accounting for the moving interface in convection/diffusion phase change. In *Numerical Methods in Thermal Problems*, ed. R. W. Lewis and K. Morgan. Pineridge Press, Swansea, 1985, **4,** 595–609.
18. Hirt, C. W. and Nichols, B. D., Volume of fluid (VOF) method for the dynamics of free boundaries. *J. Comp. Phys.*, 1981, **39,** 210–225.
19. Roache, P. J., *Computational Fluid Dynamics*. Hermosa, 1976.
20. Kurz, W. and Fisher, D. J., *Fundamentals of Solidification*. Trans Tech Publications, 1989.
21. de Vahl Davis, G., Natural convection of air in a square cavity: a bench mark solution. *International Journal of Numerical Methods in Fluids*, 1983, **3,** 249–264.
22. Özişik, M. N., *Heat Conduction*. John Wiley, 1980.
23. Yao, M., Raman, R. and de Groh III, H. C., Numerical modeling of Bridgman growth in space with MEPHISTO. In *Computational Mechanics '95, Proceedings of the International Conference on Computational Engineering Science*. Mauna Lai, Hawaii, 1995, **1,** 514–519. Springer (also NASA Tech Mem. no. 107015).
24. Dantzig, J. A., Modelling liquid–solid phase changes with melt convection. *International Journal of Numerical Methods in Engineering*, 1989, **28,** 1769–1785.
25. Thompson, M. E. and Szekely, J., Mathematical and physical modelling of double-diffusive convection of aqueous solutions crystallizing at a vertical wall. *Journal of Fluid Mechanics*, 1988, **187,** 409–433.